High pressure deformation mechanism of Li-ABW: synchrotron XRPD study and ab-initio molecular dynamic simulations

Available online at www.sciencedirect.com
ScienceDirect
Microporous and Mesoporous Materials 115 (2008) 267–280
MICROPOROUS AND MESOPOROUS MATERIALS
www.elsevier.com/locate/micromeso

High pressure deformation mechanism of Li-ABW: Synchrotron XRPD study and ab initio molecular dynamics simulations

E. Fois [a], A. Gamba [a], C. Medici [a], G. Tabacchi [a], S. Quartieri [b], E. Mazzucato [b], R. Arletti [c], G. Vezzalini [c,*], V. Dmitriev [d]

[a] *Dipartimento di Scienze Chimiche ed Ambientali, via Lucini 3, I-22100 Como, Italy*
[b] *Dipartimento di Scienze della Terra, Salita Sperone 31, I-98166 Messina, S. Agata, Italy*
[c] *Dipartimento di Scienze della Terra, Largo S. Eufemia, 19, I-41100 Modena, Italy*
[d] *Swiss-Norwegian Beam Lines at ESRF, BP220, 38043 Grenoble Cedex, France*

Received 19 November 2007; received in revised form 24 January 2008; accepted 31 January 2008
Available online 9 February 2008

Abstract

The response to compression of the synthetic zeolite Li-ABW ($LiAlSiO_4 \cdot H_2O$, $Z = 4$, *s.g.* $Pna2_1$) was explored by synchrotron X-ray powder diffraction experiments, using silicone oil as non-penetrating pressure transmitting medium, and Car Parrinello Molecular Dynamics simulations. In the range P_{amb} – 8.9 GPa, a nearly isotropic compression for the axial parameters and a cell volume decrease of approximately 12% are observed. A discontinuity in the cell parameters *vs P* behaviour can be detected between 5 and 6 GPa. As a consequence, the bulk modulus was calculated separately in the P_{amb} – 4.9 GPa and 5.6–8.9 GPa pressure ranges. The corresponding values (72(2) GPa and 80(2) GPa, respectively) are among the highest found up to now for zeolites studied with non-penetrating P-transmitting media. Molecular Dynamics simulations were performed at volumes corresponding to P_{amb}, 1.5, 5.6, and 7.6 GPa, respectively. At 1.5 GPa the channel system is already elliptically deformed, and the zig-zag trend of the 4-ring tetrahedral chains is enhanced. Moreover, the water molecule chain running along the channel becomes interrupted and the water molecules are more strongly connected to the framework oxygen atoms. The four-fold coordination of Li cation is maintained up to the highest pressure and only a slight bond distance decrease is observed above 1.5 GPa. In the P_{amb} – 5.6 GPa range, all T–O–T angles decrease with pressure, and hence the Li-ABW structure can be defined as collapsible. Otherwise, at higher compression, average T–O–T angles increase slightly. Overall, the deformation of the Li-ABW upon compression resembles that achieved by anhydrous Li-ABW in the high temperature regimes.

Keywords: Zeolite; Li-ABW; High pressure; Elastic parameters; X-ray powder diffraction; Molecular dynamics; Synchrotron radiation

1. Introduction

The applicability and efficiency of zeolites and microporous materials as catalysts, selective absorbers, and ionic exchangers can be strongly affected by the non-ambient conditions in particular, high temperature (HT) and high pressure (HP) under which they operate. As a consequence, in situ studies of their structure under "operating conditions" are essential for an understanding of the mechanisms at work when they operate as, *e.g.* nano-reactors. In particular, HP can induce structural changes, which could give rise to profound modifications to the zeolite physical properties, and hence make the material useful for new specific applications [1,2]. Moreover, the framework flexibility upon compression can modify the accessibility to the zeolite catalytic sites by the molecular species entering the porous material.

Recent HP studies (see for instance [3–11]) performed using pore-penetrating pressure transmitting media- *i.e.* potentially able to enter the framework channels and cavities, thanks to their molecular dimensions – showed that

* Corresponding author. Tel.: +39 0592055827; fax: +39 0592055887.
E-mail address: mariagiovanna.vezzalini@unimore.it (G. Vezzalini).

1387-1811/$ - see front matter © 2008 Elsevier Inc. All rights reserved.
doi:10.1016/j.micromeso.2008.01.041

zeolites can undergo irreversibile P-induced hydration, with retention of the HP phase in ambient conditions. In parallel, a relevant number of HP studies have been performed on zeolites with non-penetrating media (*i.e.* fibrous zeolites: [12–20]; analcime and wairakite: [21,22]; heulandite: [23,24]; bikitaite: [25,26]; yugawaralite: [27–29]; zeolite Y: [30]; zeolite A: [31,32]; levyne: [33]; gismondine [34]). From these investigations, the crucial role of the extra-framework content on the zeolite response – in terms of deformation mechanisms and compressibility values – emerged clearly [16,22,28,35,36].

This paper presents the results of a HP investigation, obtained combining synchrotron X-ray powder diffraction (XRPD) with ab initio Molecular Dynamics (MD) simulations, on the synthetic zeolite Li-ABW ($LiAlSiO_4 \cdot H_2O$, $Z = 4$, *s.g.* $Pna2_1$).

Li-ABW was first synthesized by Barrer and White in 1951 [37], and the framework structure and water positions were later determined by Kerr [38] by X-ray powder diffraction. The structure was then confirmed from X-ray single-crystal refinement [39] and neutron powder diffraction [40], which also gave the lithium and hydrogen positions. The ABW framework type [41] is formed by 4-, 6-, and 8-rings of TO_4-tetrahedra (see Fig. 1) and displays fully ordered Si, Al distribution. It can be described as zig-zag chains of 4-rings running along the *c*-axis of the orthorhombic unit cell ($a = 10.313(1)$, $b = 8.194(1)$, $c = 4.993(1)$ Å, from [39]). These chains are linked together forming non-crossing 8-ring channels, in which water molecules and lithium are sited. A very large number of synthetic phases with ABW framework type have been produced with several different tetrahedral and extra-framework cations (see [41] and references cited here).

Li-ABW shares a set of features with the natural zeolite bikitaite, $Li[AlSi_2O_6] \cdot H_2O$. Both are high-density zeolites – ranking around the top of the known frameworks density scale – with 100% Li as extra-framework cations, and high Si/Al ratios (2/1 in bikitaite, 1/1 in Li-ABW). Their framework topology is characterized by sheets of tetrahedra forming a hexagonal tiling, but they differ in the way each tetrahedron is connected to its neighbours in the sheet, and in the way these sheets are linked. While in bikitaite parallel sheets are connected by chains of SiO_4 tetrahedra (pyroxene chains) to form a triclinic structure [42], in Li-ABW the hexagonal sheets are directly connected to each other to form an orthorhombic frame. However, both structures contain 8-membered TO_4 rings, nearly perpendicular to the hexagonal tiling, developing mono-dimensional non-crossing channels. The main characteristic that renders such structures interesting is, however, the content of the channels system: the Li^+ cations are coordinated to three framework oxygen atoms and one water molecule oxygen, respectively. The water molecules are hydrogen-bonded to each other and form a peculiar one-dimensional chain (the one-dimensional ice structure), parallel to the channel direction. At ambient conditions, the water molecules are also weakly hydrogen-bonded to the framework oxygen atoms in the case of Li-ABW, whereas no hydrogen bond has been found between water and framework in bikitaite.

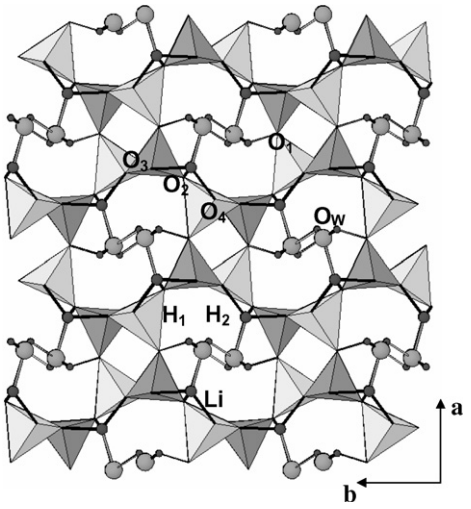

Fig. 1. Projection along [001] of Li-ABW at P_{amb}. Al: light grey tetrahedra, Si: grey tetrahedra.

Bikitaite has been studied under ambient conditions, high pressure, and high temperature, by means of both single-crystal X-ray diffraction ([25,42] and by the combined experimental-computational approach also adopted in the present work [26,43–48]. In particular, the results of the study on bikitaite under HP [25,26] confirmed that an essential role may be played by the extra-framework species in determining the deformation mechanism of this zeolite. Upon compression, the one-dimensional ice structure was not disrupted and new hydrogen bonds were formed between the previously "floating" water chains and the framework oxygen atoms. Moreover, bikitaite results much more stable and rigid under HT [47,48] than HP conditions [26,45].

The thermal behaviour of Li-ABW was investigated from the experimental point of view by Norby [49] who showed that reversible dehydration is possible to a limited extent and rehydration is only possible after prolonged hydrothermal treatments. Moreover at 650 °C the anhydrous structure is subjected to a displacive transition and collapses into the anhydrous phase γ-eucriptite [49]. Also, a computational study of the dehydrated Li-ABW was performed [50], and it was reported that Li cations play a relevant role in the displacive framework rearrangement under high temperature. Moreover, the H*T* reconstructive transformation of dehydrated Li-ABW to γ-eucriptite was simulated via the metadynamics approach [51]. However, to date no data was available on the behaviour of this porous material under pressure. Here the results of an integrated experimental-theoretical study are presented, aiming to fill this gap, and with the following main objectives: (i) to determine the baric stability of Li-ABW, (ii) to compare the HT and HP deformation mechanisms, and (iii) to compare the elastic behaviour, the *P*-induced modifications and

the host-guest interactions in Li-ABW with those in bikitaite.

2. Synchrotron X-ray diffraction experiments

The powder diffraction experiments were performed at the SNBL1 (BM01a) beamline at ESRF (European Synchrotron Radiation Facility) at a fixed wavelength of 0.7 Å, using a diamond anvil cell and silicone oil as non-penetrating *P*-transmitting medium. The sample was equilibrated for about 30 min at each measured pressure. The pressure was measured using the ruby fluorescence method [52] on the non-linear hydrostatic pressure scale [53]. The estimated error in the pressure values is 0.2 GPa. The experiment was performed from P_{amb} up to about 9 GPa, with ΔP increments of 0.5–1 GPa. Due to a technical limitation that occurred during the experiment, no patterns were collected while decompressing the sample. A MAR345 detector (pixel dimension 150 μm) was used at a fixed distance of 330 mm from the sample; the exposure time was 1200 s for all pressure points. One-dimensional diffraction patterns were obtained in the 2θ range 0–37° by integrating the two dimensional images with the program FIT2D [54] and are reported in Fig. 2.

As already found in other studies by our group (see for instance [14,22,28,34]), the peak intensities of the collected

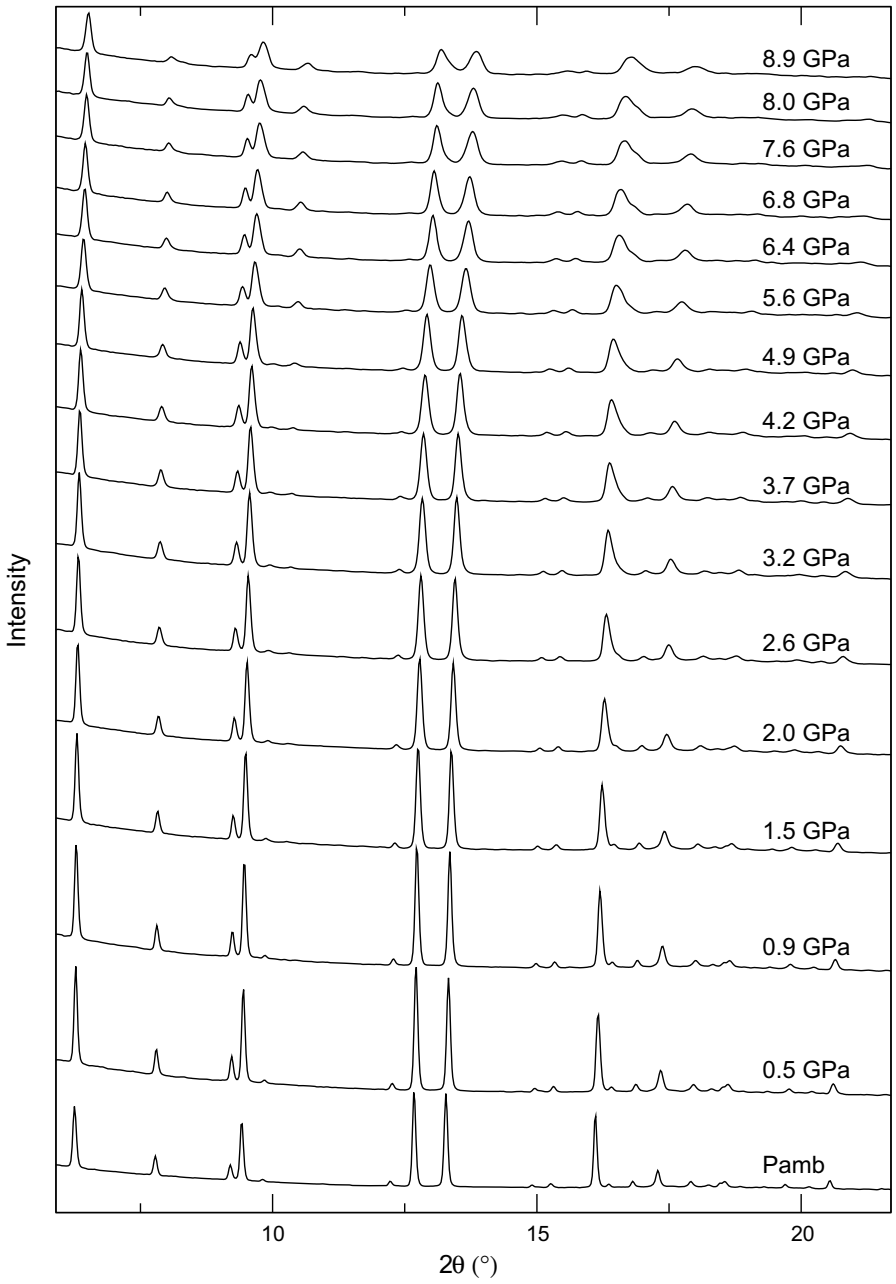

Fig. 2. Selected integrated XRD powder patterns of Li-ABW in silicone oil as a function of pressure.

Table 1
Unit cell parameters of Li-ABW at the investigated pressures

P (GPa)	a (Å)	b (Å)	c (Å)	V (Å^3)
P_{amb}	10.313(2)	8.186(2)	4.9951(8)	421.7(2)
0.5	10.283(1)	8.150(2)	4.9779(7)	417.2(2)
0.9	10.272(1)	8.139(2)	4.9673(7)	415.3(2)
1.5	10.254(1)	8.122(1)	4.9545(5)	412.64(6)
2.0	10.230(1)	8.099(1)	4.9392(7)	409.22(6)
2.6	10.213(1)	8.080(1)	4.9279(8)	406.65(7)
3.2	10.195(1)	8.061(2)	4.9169(9)	404.08(8)
3.7	10.175(1)	8.041(2)	4.905(1)	401.37(8)
4.2	10.156(2)	8.019(2)	4.897(1)	398.83(9)
4.9	10.130(2)	7.990(2)	4.887(1)	395.5(1)
5.6	10.079(2)	7.937(2)	4.866(1)	389.3(1)
6.4	10.038(2)	7.913(3)	4.851(1)	385.3(1)
6.8	10.016(2)	7.897(3)	4.844(2)	383.1(1)
7.6	9.973(3)	7.871(3)	4.822(2)	378.5(1)
8.0	9.962(5)	7.864(5)	4.816(2)	377.3(5)
8.9	9.899(5)	7.849(6)	4.789(2)	372.1(5)

patterns are often not reliable, since they are significantly influenced by a number of uncontrollable effects, such as the poor statistics of the diffraction data – due to the low mosaicity of the crystallites and the small volume hit by the beam – and the possible development of strong preferred orientations. As a consequence, crystal structure refinements are prevented and only the unit cell parameters were extracted from the powder patterns by means of the Rietveld method. The unit cell refinements were carried out in the 2θ range 5–25° up to 8.9 GPa, using the computer program GSAS [55] with the EXPGUI interface [56]. The background curves were fitted by a Chebyshev polynomial. The pseudo-Voigt profile function proposed by Thomson and co-workers [57,58] was used. The refined cell parameters as a function of pressure are reported in Table 1 and in Fig. 3. The isothermal bulk modulus was determined by the EOS-FIT program [59,60].

3. Computational methods and simulation models

The calculations were performed by adopting a fixed volume approach, using the experimentally detected cell parameters data (see Table 1). Simulations were performed for four different cell parameter data sets. The corresponding pressure values were, respectively, P_{amb}, 1.5 GPa, 5.6 GPa and 7.6 GPa (Table 1). The simulation cell corresponded to two crystallographic unit cell, specifically the simulation cell size was twice the crystallographic cell along the c-axis, the direction of the non-crossing 8-membered ring channel (the direction along which the water chain develops). Accordingly, the stoichiometry of the simulated Li-ABW cell corresponds to $Li_8[Al_8Si_8O_{32}](H_2O)_8$. The simulations were performed by using the first-principles molecular dynamics (Car Parrinello) method [61], and periodic boundary conditions were adopted. The density functional theory (DFT) approximation [62] adopted here for the solution of the electronic problem was a gradient-corrected DFT approximation using the Becke [63] and Perdew [64] (BP) functionals. A plane wave basis set was also used, and a cutoff of 60 Ry was adopted for the expansion of the electronic states. Only valence electrons were explicitly accounted for, and ionic core electron interactions were computed via Norm Conserving Pseudopotential, adopting the semilocal Kleinman and Bylander method [65]. Atomic pseudopotentials were obtained using the Troulliers and Martins scheme [66]. Non-locality up $l = 2$ (d-non-locality) was used for Si, Al and O atoms, p-non-locality was used for Li, while a local pseudopotential was used for H atoms. The equations of motion were integrated [66] using a time step of 0.121 fs, while an inertia parameter of 500 a.u. was used for the electronic part in the Car Parrinello equations. The NVT ensemble was applied for the finite temperature simulations (*i.e.* with constant number of particles N, volume V and temperature T). Temperature was controlled by a chain of Nose-Hoover thermostats [67], using 300 K as target temperature. Besides the constant NVT, no other constraints were imposed on the system, and so all atoms were left free to move without symmetry constraints. The CPMD code was used in this study [68]. This type of calculation set-up is the same adopted by our group in studies of response-to-compression behaviour in zeolites [26,28,29,34,46], in many other simulations concerning zeolites at ambient conditions [42–45,69–72] and other framework minerals [73]. In particular it is the same approach adopted in the study of both ambient conditions [44] and HT properties of Li-ABW [50]. Trajectories were performed for an elapsed time of about 10 ps for each of the four studied cell volumes extracted from the experimental P/V curve. Each run was equilibrated for 4 ps at room temperature, then data was averaged from the following 6 ps production trajectories. Average atomic position was calculated. It turned out that the group symmetry ($Pna2_1$) was satisfied by the atomic average position even if no constraint was imposed except the cell parameters. Atomic thermal parameters (Beq) were also calculated. Atomic coordinates and Beq obtained from the four simulations at different volumes are reported in Table 2. Inter-atomic distances and angles were obtained by averaging the instantaneous distances and angles calculated along the trajectories and they will be used as basis for the discussion. In addition, pair distribution functions ($g(r)$'s) were calculated. For the sake of simplicity, the simulations, even performed at constant volume, will often be referred to the corresponding experimental pressure.

4. Results

4.1. Elastic behaviour

Fig. 2 reports selected experimental powder patterns of Li-ABW as a function of pressure. The peak intensities generally decrease and the peak profiles become broader with increasing pressure, as a consequence of both the

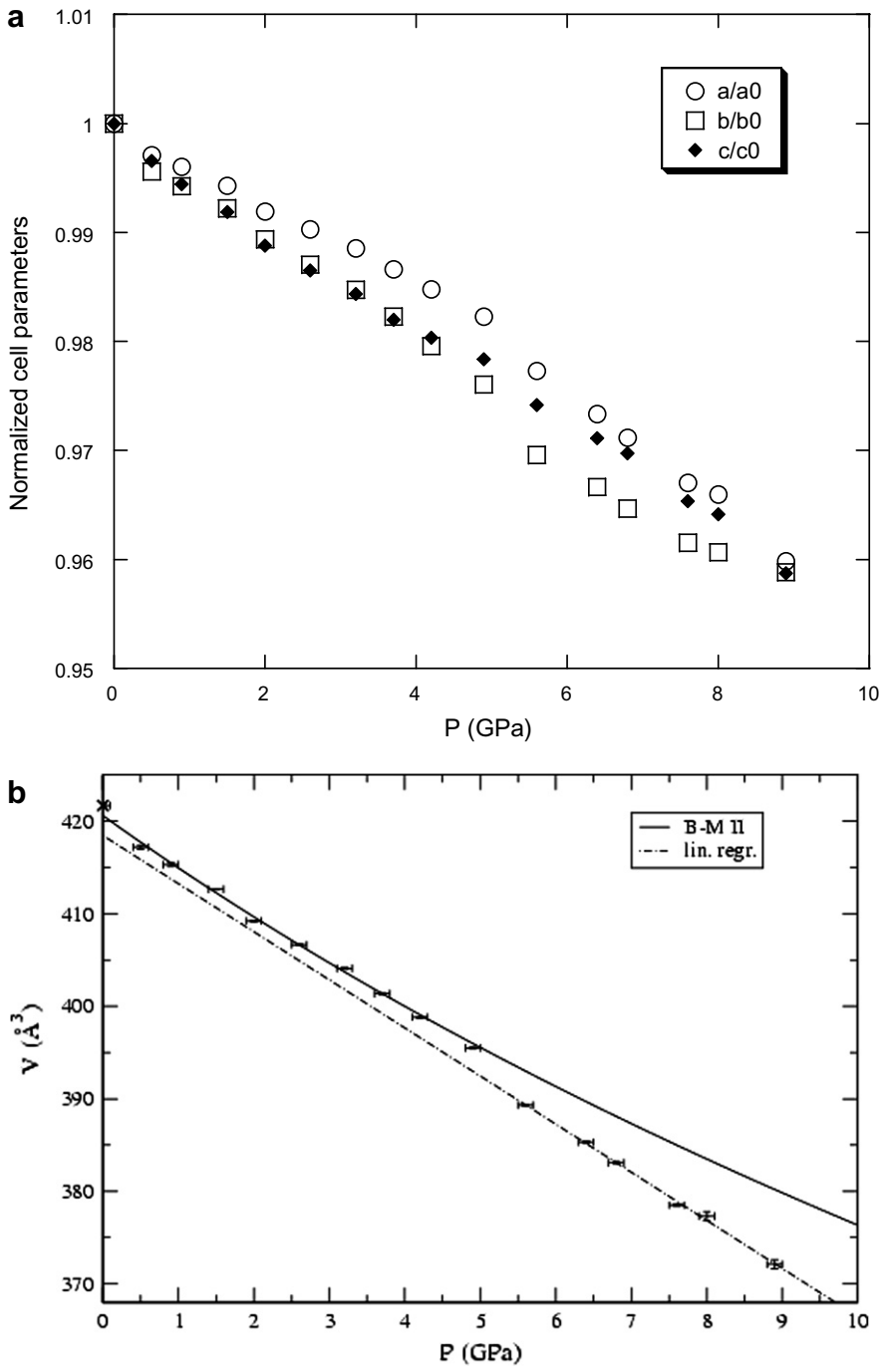

Fig. 3. (a) Unit cell parameters of Li-ABW, normalized to room condition values, *vs.* pressure. (b) Unit cell volume *vs.* pressure; solid line: fit obtained using a second-order Birch–Murnaghan EoS; dotted line: linear fit.

increase in the long range structural disorder, and the presence of microstrains caused by deviatoric stress in the non-hydrostatic *P*-transmitting medium [74–77]. The HP XRPD data demonstrates that Li-ABW does not undergo complete X-ray amorphization up to the highest investigated pressure. Fig. 3a and b and Table 1 show an isotropic contraction of the axial parameters (of about 4%) and an overall reduction of about 12% of the unit cell volume in the whole investigated *P* range. From Fig. 3, a discontinuity in the cell parameters *vs P* trend can be detected between 5 and 6 GPa. As a consequence, the bulk modulus was calculated separately in the following two *P*-ranges: P_{amb} – 4.9 GPa and 5.6–8.9 GPa (Fig. 3b). The low-*P* data were fitted with a second-order Birch–Murnaghan Equation of State (II-BM-EoS, [60]) using the EOS-Fit V5.2 program [59]. The first point, corresponding to the experimental volume at P_{amb}, was excluded being significantly out of trend. The elastic parameters, obtained using the data weighted by the uncertainties in *P* and *V*, are $V_0 = 420.6(4)$ Å^3, $K_0 = 72(2)$ GPa.

Table 2
Li-ABW crystallographic atomic coordinates and isotropic thermal factors Biso (in Å^2) from ab initio MD simulations at different pressures

	x	y	z	B_{iso}
P_{amb}				
Li	0.1654	0.6543	0.2473	1.799
Al	0.1627	0.0659	0.2499	0.411
Si	0.3621	0.3572	0.2484	0.390
O1	0.0154	0.1675	0.1886	1.002
O2	0.2892	0.1945	0.1332	0.938
O3	0.1916	0.0215	0.5949	0.900
O4	0.1714	0.1230	0.0682	0.763
Ow	0.5180	0.0879	0.2231	3.494
H1	0.5566	0.1656	0.8599	10.745
H2	0.5566	0.0547	0.6456	12.962
1.5 GPa				
Li	0.1548	0.6344	0.2424	1.488
Al	0.1658	0.0573	0.2521	0.297
Si	0.3666	0.3477	0.2509	0.254
O1	0.0217	0.1698	0.1892	0.847
O2	0.2975	0.1803	0.1349	0.681
O3	0.1921	0.0122	0.6003	0.790
O4	0.1662	0.1351	0.0738	0.665
Ow	0.5331	0.0944	0.2036	2.922
H1	0.5539	0.1746	0.9300	3.109
H2	0.5847	0.0823	0.6829	11.044
5.6 GPa				
Li	0.1463	0.6197	0.2392	1.938
Al	0.1683	0.0515	0.2528	0.415
Si	0.3698	0.3420	0.2512	0.359
O1	0.0265	0.1721	0.1857	1.356
O2	0.3024	0.1722	0.1288	0.830
O3	0.1919	0.0095	0.6057	1.227
O4	0.1627	0.1449	0.0777	1.016
Ow	0.5437	0.0987	0.2108	4.253
H1	0.5593	0.1818	0.9235	3.844
H2	0.5930	0.0885	0.6828	13.030
7.6 GPa				
Li	0.1349	0.6072	0.2354	1.462
Al	0.1774	0.0462	0.2509	0.431
Si	0.3730	0.3406	0.2505	0.298
O1	0.0329	0.1727	0.1951	0.965
O2	0.3071	0.1720	0.1152	0.557
O3	0.1905	0.0126	0.6135	0.694
O4	0.1622	0.1526	0.0801	0.754
Ow	0.5611	0.1115	0.2108	2.068
H1	0.5607	0.1945	0.9411	2.107
H2	0.6031	0.1697	0.6481	5.919

In the pressure range from 5.6 to 8.9 GPa, due to the low number of experimental observations (six) and the restricted P range (about 3 GPa), no EOSs were able to correctly fit the experimental data. As a consequence, the bulk modulus was calculated by the following procedure: by extrapolating the experimental data with a linear regression, a V_0 value of 418.5(9) Å^3 was obtained; then, the compressibility was determined as the slope of the V/V_0 *vs.* P trend (Fig. 3b). The corresponding K_0 is 80(2) GPa. The two bulk modulus values determined here for Li-ABW are among the highest up to now found for zeolites studied with non-penetrating pressure transmitting media [12–34].

5. Atomistic interpretation of the deformation mechanism

5.1. Framework

A graphical representation of the effects of compression on the Li-ABW framework is shown in Figs. 4–6, which report the projections along the cell axes of the structures, as obtained by the simulations at different cell volumes; pictures are drawn using the calculated coordinates, averaged along the trajectories (Table 2). In the structure obtained from the simulation with the cell parameters corresponding to $P = 1.5$ GPa, the channels running along the c axis are already slightly deformed with respect to the P_{amb} one (Fig. 4). Such deformations are more pronounced at the cell volume corresponding to $P = 7.6$ GPa, in agreement with the contractions of both a and b parameters. This combined effect on both axes is consistent with the alternate diagonal orientation of the elliptic 8-ring channels. The channel deformation can be evaluated by the O_{frame}–O_{frame} distances (O_f–O_f in the following), which define the longest and the shortest axes of the 8-membered ring elliptical channel (see Table 3). A systematic increase of the channel ellipticity with compression (indicated by the increasing of the largest/shortest axis ratio) is evident.

From Fig. 5, it can be seen that the slight shift present at P_{amb} between the sheets of hexagonal rings – linked along a-axis – is enhanced by compression. Fig. 6 shows the zig-zag 4-ring chains, almost linearly developing along c-axis at P_{amb}. Upon compression, these chains become significantly distorted in the (1 0 1) plane and more zig-zag deformed. These two deformation effects further contribute to the contraction of the c parameter (Fig. 3).

The calculated average T–O–T angles values are reported in Table 4, while the T–O–T angle distributions are shown in Fig. 7a. The P_{amb} T–O–T distribution is characterized by a two-peaks profile, coalescing to a unimodal distribution at 5.6 GPa. The T–O–T angle distribution becomes multimodal at 7.6 GPa (see Fig. 7a). Both average values and distributions indicate that up to volumes corresponding to 5.6 GPa, all the T–O–T angles decrease due to the co-rotation of the tetrahedra [78]; in contrast, upon further compression (above 5.6 GPa), some T–O–T angles increase and some decrease. In particular, it is the T–O–T angle involving the O1 framework oxygen that shows the largest increase in that range of compression (see Table 4). On the other hand, the T–T–T angles (Fig. 7b) decrease only slightly with compression, from 110.6° at P_{amb} to 109.8° at 7.6 GPa.

The pair distribution functions ($g(r)$) concerning the Al–O_f and Si–O_f pairs are reported in Fig. 8. It emerges that the T–O bond lengths are practically unaffected by compression (the first peak position does not vary). On the other hand, the second nearest neighbour distances of both the Al–O_f and Si–O_f pairs, shorten with compression. In fact, the structure of the TO_4 units are practically unaffected by compression: a volume contraction of only 0.05% and 0.08% are calculated for the SiO_4 and AlO_4 tet-

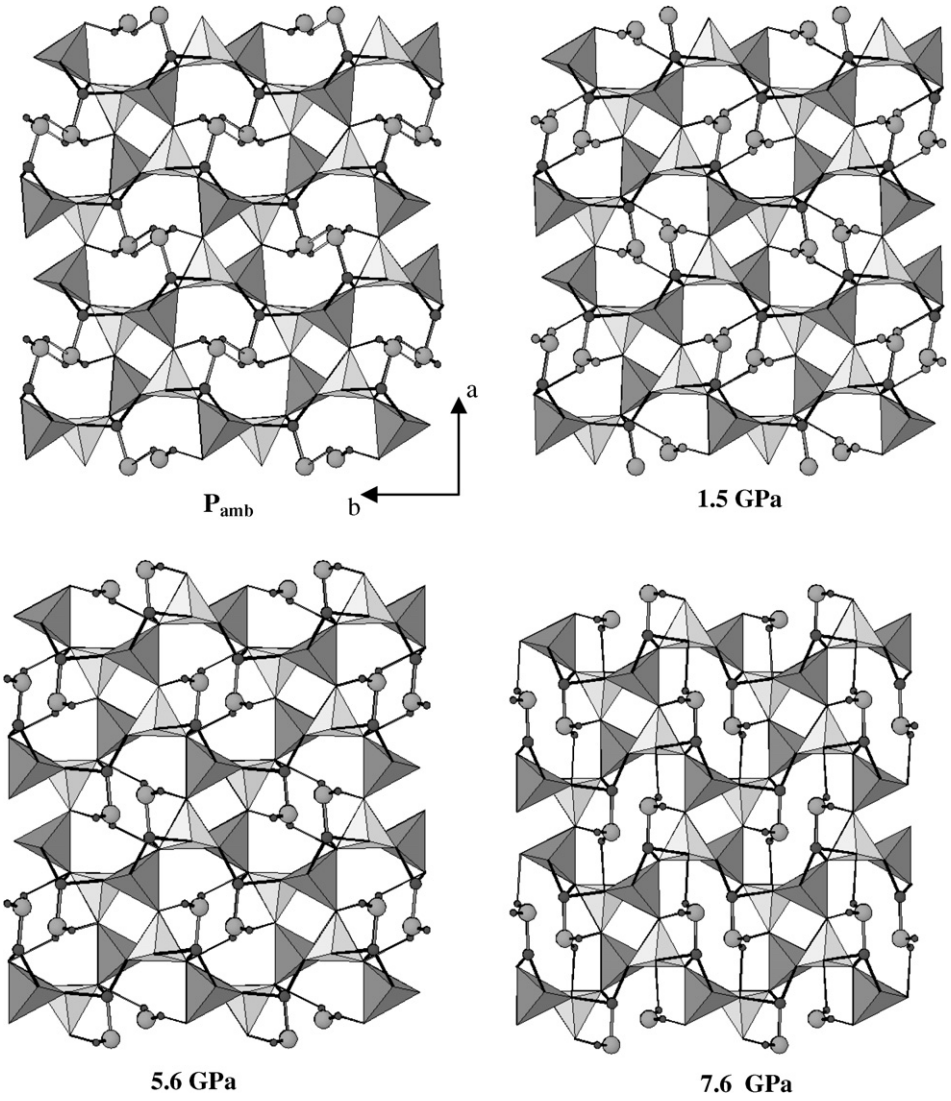

Fig. 4. Projection along [0 0 1] of Li-ABW structure at: P_{amb}, 1.5 GPa, 5.6 GPa, 7.6 GPa. Si: light grey tetrahedra, Al: grey tetrahedra.

rahedral units, respectively, for the simulation at 7.6 GPa. Since, at that pressure, the total volume contraction of the Li-ABW unit cell (about 12%) is much higher than the tetrahedral units contraction, the main cause of the P-induced structural modifications are the rotations of the quasi-rigid tetrahedral units: the mean bridging inter-tetrahedra T–O–T angles become smaller as the volume decreases up to 5.6 GPa. These findings are in agreement with what is generally observed for many other framework silicates under pressure [16,27,79] and allows us to define the Li-ABW framework as collapsible up to 5.6 GPa, on the basis of the rigid unit model [78,80–84].

5.2. Rearrangements of the extra-framework species

As reported in previous studies on Li-ABW at ambient conditions [44,71], water molecules were shown to have a certain degree of rotational disorder. This rotational disorder was confirmed in the present simulation at P_{amb}. However, this type of rotational water motion was greatly hindered by compression, and it had already disappeared in the simulation corresponding to 1.5 GPa.

Compression also affects the supramolecular structure of the caged water system (see Table 5). Fig. 6 clearly shows the effect of volume reduction on the one-dimensional hydrogen-bonded water molecule chain, which develops along the channel direction at P_{amb}. The $g(r)$'s corresponding to the O_w–O_w, O_w–O_f, H–O_w and H–O_f pairs are reported as a function of compression in Fig. 9. A peak in the H–O_w $g(r)$ centred at about 1.80 Å indicates a strong inter-water hydrogen bond at ambient conditions. Such a characteristic peak disappears already at 1.5 GPa, indicating the breaking of the hydrogen bonded water chain (Fig. 6). On the other hand, the first peak in the H–O_f $g(r)$, which is found at about 1.90 Å in ambient conditions, becomes stronger and shifted to smaller distance with compression (1.66 Å at 7.6 GPa). These facts indicate that, while the water–water hydrogen bonds disappear

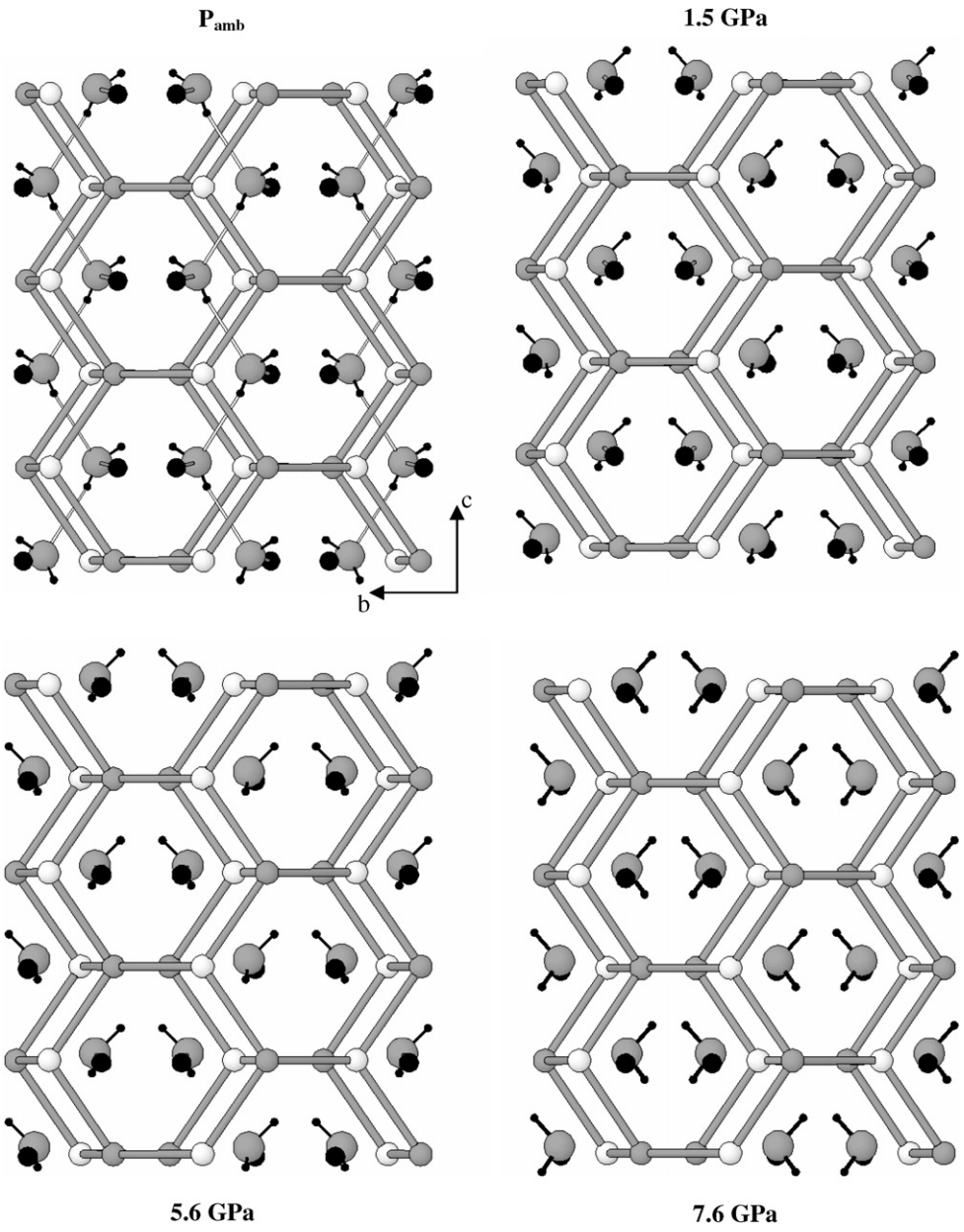

Fig. 5. Stick-and-ball drawing of Li-ABW structure projected along [1 0 0] at: P_{amb}; 1.5 GPa; 5.6 GPa; 7.6 GPa. Al light grey circles; Si grey circles; Li large black circles; OW large grey circles; H small black circles.

upon compression, the water–framework oxygen interactions become stronger. These findings are also confirmed by the O_w–O_w and O_w–O_f $g(r)$'s: upon compression, the first peak of the former is shifted at longer distances while the same peak in the latter is shifted at shorter distances.

The rearrangement of the hydrogen bonding pattern is the response of the water molecules system to the channel squashing, which moves the water molecules towards the channel walls, with the progressive increase of the mean water–water distance (from 2.94 Å at P_{amb} to 3.23 Å at 7.6 GPa, see Table 5 and Fig. 9). Also, a rearrangement of the host/guest hydrogen bond structure occurs along the compression path. While one of the water hydrogen atoms gets closer to the framework oxygen O1 as a function of compression, the second water proton gets close to O2 at 1.5 GPa, when the water–water hydrogen bonding system is disrupted. Successively, in passing from 5.6 GPa to 7.6 GPa, this second proton becomes involved in an alternative hydrogen bond contact with O4 (Table 5).

In the whole studied compression range, the Li cation remains four-fold coordinated, to three framework oxygen atoms (O2, O3, O4) and one water molecule, Ow (Table 6). It is worth noting that Li coordination distances are almost independent of pressure. In contrast, we observe significant variations in the internal bond angles of the Li tetrahedron, which become progressively more distorted with increasing

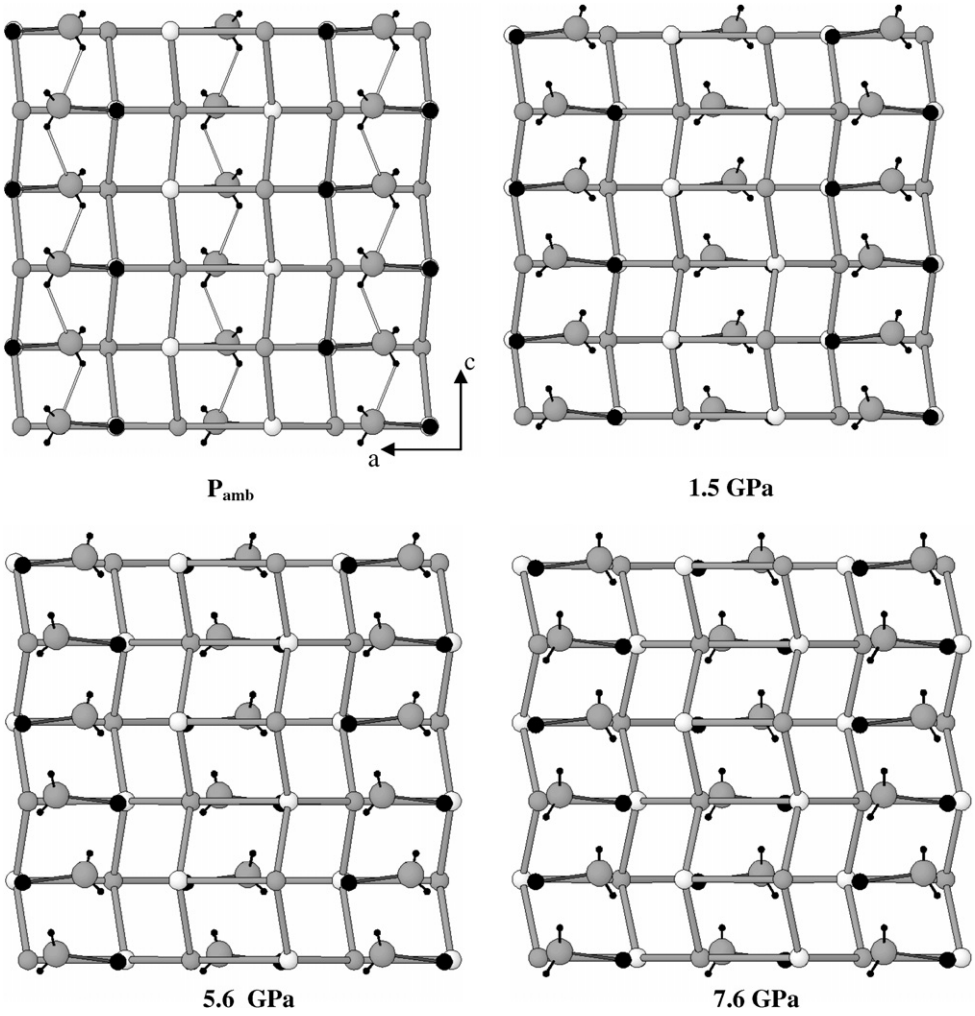

Fig. 6. Stick-and-ball drawing of Li-ABW structure projected along [0 1 0] at: P_{amb}; 1.5 GPa; 5.6 GPa; 7.6 GPa. Al light grey circles; Si grey circles; Li large black circles; OW large grey circles; H small black circles.

Table 3
Calculated average O–O distances defining the longest and shortest axes of the elliptic 8-ring channel aperture in Li-ABW as a function of compression, determined by ab initio MD simulations

	P_{amb}	1.5 GPa	5.6 GPa	7.6 GPa	650° anhydr.
Longest axis	8.19 (0.21)*	8.38 (0.12)	8.38 (0.12)	8.36 (0.13)	9.38
Shortest axis	5.95 (0.22)	5.65 (0.11)	5.42 (0.11)	5.29 (0.11)	3.96
Ratio	1.38	1.48	1.55	1.58	2.37

Standard deviations (sd) are in parentheses. Both distances and sd's are in Å. Also shown are the corresponding distances from the high temperature simulation of dehydrated Li-ABW (650° anhydr.) [50].

* The sd's reported in the tables are not standard errors, but represent a measure of the finite temperature fluctuations of the distances along the trajectory, determined by the thermal motion of the atoms.

Table 4
Calculated average T–O–T angles obtained at different degrees of compression by ab initio MD simulations

	P_{amb}	1.5 GPa	5.6 GPa	7.6 GPa
Al–O1–Si	137.8 (6.4)	137.0 (5.8)	134.9 (6.4)	141.9 (4.7)
Al–O2–Si	134.2 (4.6)	132.2 (4.3)	129.4 (4.9)	127.3 (4.7)
Al–O3–Si	123.5 (4.5)	122.8 (3.6)	120.8 (4.7)	121.4 (4.6)
Al–O4–Si	124.0 (4.2)	123.1 (3.8)	121.4 (4.1)	124.3 (3.9)
<TOT>	129.9 (4.9)	128.8 (4.4)	126.6 (5.1)	128.7 (4.5)
TOT	130.0	128.9	126.9	127.2

The first four lines contain the individual T–O–T angle figures averaged during the simulations, and their respective standard deviations in parenthesis. The fifth line contains the grand average of the T–O–T angles. The last line reports the T–O–T angles calculated from the average atomic positions.

pressure (Table 6). Such a distortion is due to two main reasons. The first is related to the fact that the framework oxygen O1 is the only framework oxygen not coordinated to Li and is only weakly interacting (*via* hydrogen bond) with water at P_{amb}. Upon compression, such a hydrogen bond becomes stronger and induces a shortening of the Ow–O1 distance (Table 5), bringing about a distortion of the Li tetrahedron. Moreover, the second-nearest water oxygen (labelled Ow′ hereafter and in Table 6) gets closer to Li at 7.6 GPa. As a consequence, the structure of the

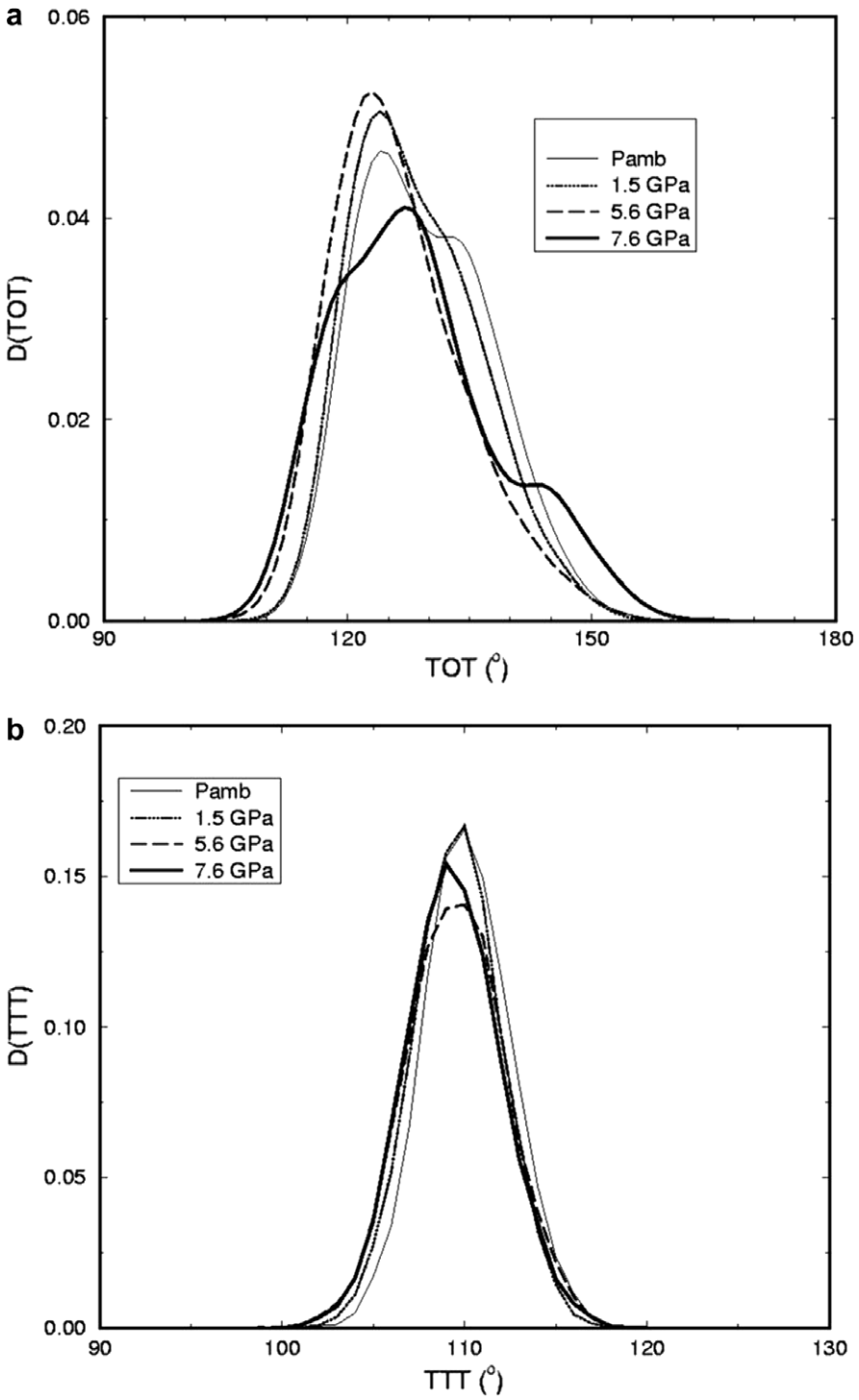

Fig. 7. (a) Normalized distribution D(TOT) of the T–O–T angles from the ab initio Molecular Dynamics simulations at the volume corresponding to P_{amb}, 1.5 GPa, 5.6 GPa and 7.6 GPa. (b) Normalized distribution D(TTT) of the T–T–T angles from the ab initio molecular dynamics simulations at the volume corresponding to P_{amb}, 1.5 GPa, 5.6 GPa, and 7.6 GPa.

Li polyhedron – which is close to tetrahedral at ambient conditions – becomes more distorted with increasing P, so coming to resemble a trigonal bipyramid. The fifth vertex of this Li-centred polyhedron is Ow′, which, however, cannot be considered as coordinated to Li, due to the excessive Li–Ow′ distance (2.86 Å at 7.6 GPa).

6. Discussion

6.1. HT vs. HP deformation mechanism of Li-ABW

It is interesting to compare the HP vs. HT deformation mechanism of the Li-ABW structure. The Li-ABW HT

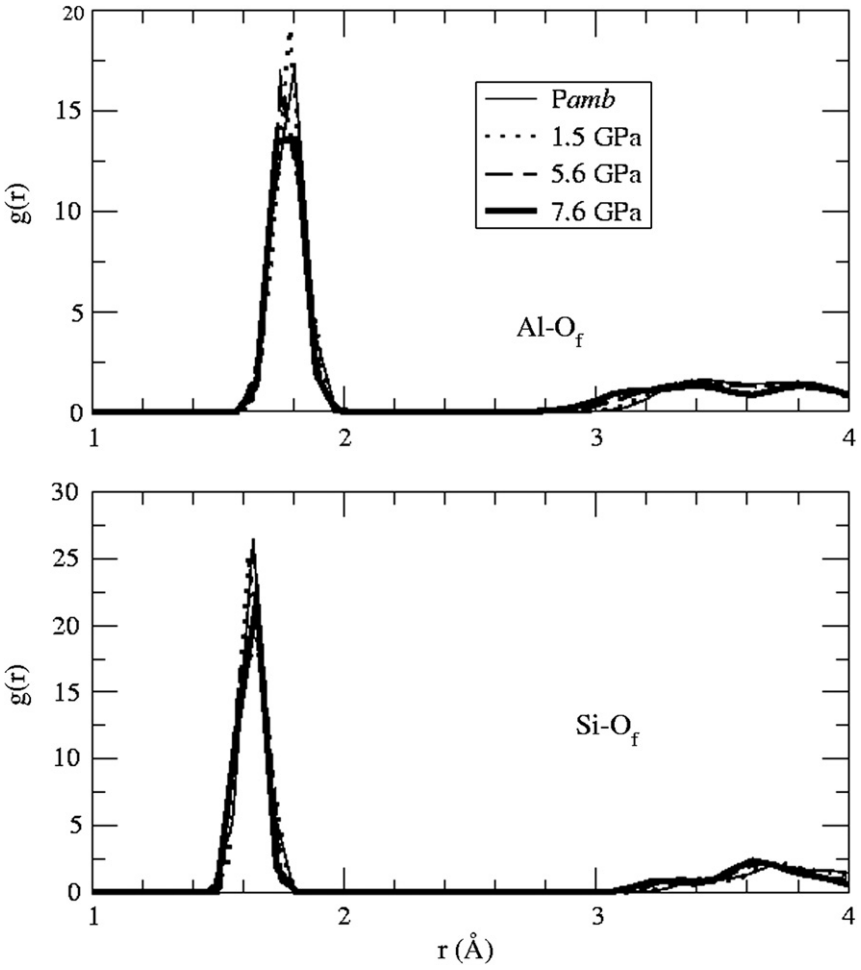

Fig. 8. Pair distribution functions $g(r)$ for Ow–Ow, Of–Ow, H–Ow, and H–Of pairs from the ab initio Molecular Dynamics simulations at the volume corresponding to P_{amb}, 1.5 GPa, 5.6 GPa, and 7.6 GPa.

Table 5
Calculated average intra-molecular water distances (and standard deviations (sd) in parenthesis) and relevant water–water, water–Li, water–framework oxygen distances as a function of compression, determined by ab initio MD simulations

	P_{amb}	1.5 GPa	5.6 GPa	7.6 GPa
Ow–H1	0.99 (0.04)	1.00 (0.04)	0.99 (0.04)	1.00 (0.04)
Ow–H2	0.98 (0.04)	0.99 (0.04)	0.99 (0.06)	1.00 (0.03)
Ow–Li	2.01 (0.21)	2.00 (0.29)	1.98 (0.20)	1.98 (0.24)
Ow–Ow	2.94 (0.42)	3.08 (0.38)	3.07 (0.45)	3.23 (0.45)
Ow–O1	2.88 (0.32)	2.76 (0.25)	2.69 (0.22)	2.62 (0.18)
H1–O1	2.21 (0.93)	1.85 (0.31)	1.78 (0.35)	1.66 (0.23)
H2–O2	–	2.23 (0.30)	2.03 (0.32)	–
H2–O4	–	–	–	2.09 (0.25)

Distances and sd's in Å.

behaviour has been investigated both experimentally [49] and in simulations [50,51]. At 650 °C the system is completely dehydrated and its volume is contracted by about 20% [49], moreover a decrease of the average T–O–T angle is also detected [50,51]. Furthermore, the 8-membered ring becomes more elliptical at HT (Table 3). The microscopic behaviour indicates that the under-saturation of framework oxygen O1 may be the cause of the details of the T-induced framework deformation. Indeed, as water leaves Li-ABW channels, O1 is completely "naked", and Li is reported to split its position becoming disordered in two sites, the new one being closer to O1 [50]. Such a HT Li positional disorder has been found to trigger the Li-ABW to γ-eucriptite phase change [51]. On the whole, the Li-ABW HT framework deformation resembles the one described here upon compression: a substantial volume decrease, a more elliptical one-dimensional channel accompanied by a decrease of T–O–T angles, while TO_4 units are practically unaffected by both high P and T. Moreover, in both cases, O1 coordination plays a relevant role.

6.2. Comparison between Li-ABW and bikitaite compression behaviour

Li-ABW and bikitaite are characterized by an identical extra-framework species content, namely Li as extra-framework cation and a mono-dimensional water chain in the non-crossing 8-membered ring. The HP-induced volume contraction of Li-ABW and bikitaite [26] are rather

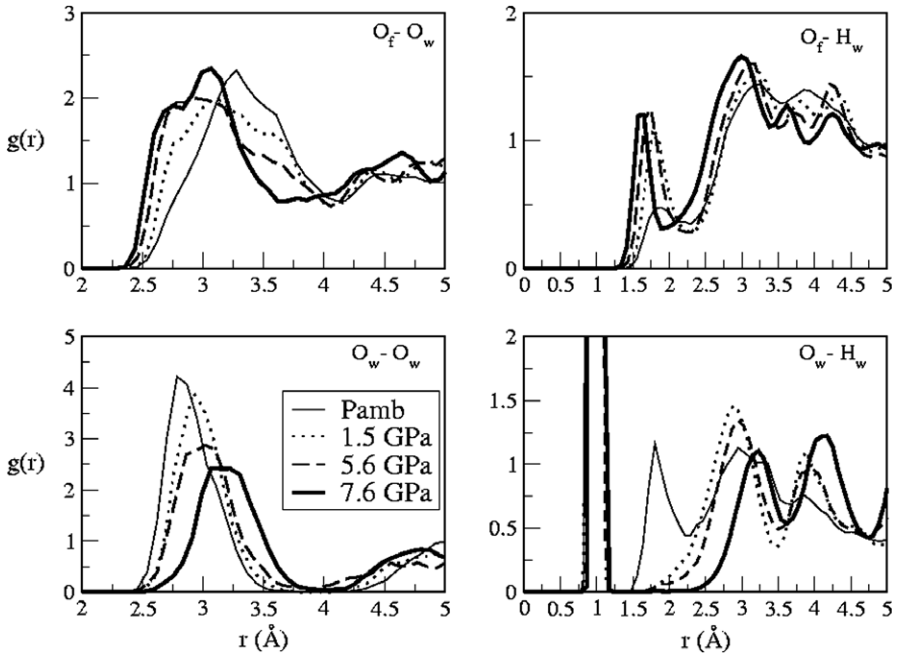

Fig. 9. Pair distribution functions $g(r)$ for Al–Of and Si–Of pairs from the ab initio Molecular Dynamics simulations at the volume corresponding to P_{amb}, 1.5 GPa, 5.6 GPa, and 7.6 GPa.

Table 6
Average coordination distances and O–Li–O angles of Li polyhedron at different compression determined by ab initio molecular dynamics

	P_{amb}	1.5 GPa	5.6 GPa	7.6 GPa
Li–O2	2.02 (0.23)	2.05 (0.23)	2.02 (0.20)	2.00 (0.23)
Li–O3	2.00 (0.20)	2.00 (0.17)	1.98 (0.19)	2.00 (0.19)
Li–O4	2.05 (0.24)	2.06 (0.22)	1.80 (0.22)	2.06 (0.26)
Li–Ow	2.01 (0.21)	2.00 (0.20)	1.98 (0.20)	2.00 (0.19)
Li–O1	3.22 (0.29)	3.28 (0.24)	3.26 (0.27)	3.23 (0.28)
Li–Ow′	3.45 (0.60)	3.15 (0.56)	3.00 (0.727)	2.86 (0.54)
O2–Li–O3	106.1 (6.3)	103.6 (5.9)	100.9 (6.5)	96.3 (6.2)
O2–Li–O4	105.2 (6.4)	101.9 (6.3)	98.8 (6.4)	93.5 (6.5)
O2–Li–Ow	101.0 (8.8)	97.6 (6.5)	98.6(7.2)	99.0 (6.7)
O3–Li–O4	107.0 (6.6)	97.6 (6.3)	98.6 (7.2)	99.0 (6.4)
O3–Li–Ow	125.4 (11.1)	136.7 (9.9)	143.8 (12.5)	153.9 (9.5)
O4–Li–Ow	107.1 (7.8)	104.7 (7.6)	101.5 (8.0)	99.1 (7.4)

Distances in Å, angles in degrees. In parenthesis the calculated standard deviations.

similar (12% and 15%, respectively, in the pressure range P_{amb} – 9 GPa). MD simulations on compressed bikitaite show that the peculiar "floating" one-dimensional water chain is not destroyed, but only partially perturbed by high pressure. The compression brings framework oxygen atoms close enough to water hydrogen atoms to allow the formation of new host-guest hydrogen bonds, without, however, destroying the one-dimensional chain [26]. In contrast, in Li-ABW the water chain, which is weakly connected to the framework already at P_{amb}, is interrupted at 1.5 GPa and the water molecules are much more strongly bonded to the framework oxygen atoms (Fig. 4).

As regards the Li polyhedron at HP, the mean Li–O bond distance and the polyhedral volume in bikitaite decrease, without significant distortions of the internal tetrahedral angles. In Li-ABW we observe an opposite deformation behaviour: the Li coordination distances are quite constant while the internal tetrahedral angles undergo larger distortions, due to the displacement of the water molecule with respect to Li inside the channel (Table 6). Moreover, while in bikitaite, the T–O–T angles regularly decrease with compression, in Li-ABW this T–O–T angles behaviour holds only up to 5.6 GPa. Following Baur's definition of collapsible framework (decrease of all T–O–T angles with volume contraction [78]), bikitaite can be considered collapsible in all the studied P range, while Li-ABW can be considered collapsible only up to 5.6 GPa. At higher pressures, calculations indicate changes in the hydrogen bonding system, which occur in parallel with the increase in most of the T–O–T angles. This can explain the variations in the elastic behaviour of Li-ABW observed between 5 and 6 GPa (Fig. 3), more evident for the unit cell parameters than for the unit cell volume.

Acknowledgments

This work was supported by the Italian MIUR (PRIN2006 "Zeolites at non-ambient conditions: theoretical-experimental characterization and novel technological applications"). The Swiss-Norwegian beamline (BM01) at the European Synchrotron Radiation Facility is acknowledged for allocation of beamtime and for technical support during the experiments. Dr. Diego G. Gatta (Università di Milano) is acknowledged for the helpful discussion on the bulk modulus calculation.

References

[1] R.A. Secco, S.V. Goryainov, Y. Huang, Phys. Stat. Solid. (b) 242 (2005) 73.
[2] S.V. Goryainov, R.A. Secco, Y. Huang, H. Liu, Physica B 390 (2007) 356.
[3] Y. Lee, J.A. Hriljac, T. Vogt, J.B. Parise, G. Artioli, J. Am. Chem. Soc. 123 (2001) 12732.
[4] Y. Lee, T. Vogt, J.A. Hriljac, J.B. Parise, G. Artioli, J. Am. Chem. Soc. 124 (2002) 5466.
[5] Y. Lee, T. Vogt, J.A. Hriljac, J.B. Parise, J.C. Hanson, S.J. Kim, Nature 420 (2002) 485.
[6] Y. Lee, J.A. Hriljac, T. Vogt, Phys. Chem. Miner. 31 (2004) 421.
[7] Y. Lee, J.A. Hriljac, J.B. Parise, T. Vogt, Am. Mineral. 90 (2005) 252.
[8] Y. Lee, J.A. Hriljac, J.B. Parise, T. Vogt, Am. Mineral. 91 (2006) 247.
[9] A.Yu. Likhacheva, Y.V. Seryotkin, A.Yu. Manakov, S.V. Goryainov, A.I. Ancharov, M.A. Sheromov, High Pressure Res. 26 (2006) 449–453.
[10] A.Yu. Likhacheva, Y.V. Seryotkin, A.Yu. Manakov, S.V. Goryainov, A.I. Ancharov, M.A. Sheromov, Am. Mineral. 92 (2007) 1610.
[11] M. Colligan, Y. Lee, T. Vogt, A.J. Celestian, J.B. Parise, W.G. Marshall, J.A. Hriljac, J. Phys. Chem. B 109 (2005) 18223.
[12] I.A. Belitsky, B.A. Fursenko, S.P. Gabuda, O.V. Kholdeev, Yu.V. Seryotkin, Phys. Chem. Miner. 18 (1992) 497.
[13] S.V. Goryainov, M.B. Smirnov, Eur. J. Mineral. 13 (2001) 507.
[14] P. Ballone, S. Quartieri, A. Sani, G. Vezzalini, Am. Mineral. 87 (2002) 1194.
[15] P. Comodi, G.D. Gatta, P.F. Zanazzi, Eur. J. Mineral. 14 (2002) 567.
[16] D.G. Gatta, Eur. J. Mineral. 17 (2005) 411.
[17] G.D. Gatta, T. Boffa Ballaran, P. Comodi, P.F. Zanazzi, Am. Mineral. 89 (2004) 633.
[18] G.D. Gatta, T. Boffa Ballaran, P. Comodi, P.F. Zanazzi, Phys. Chem. Miner. 31 (2004) 288.
[19] S.V. Goryainov, A.V. Kursonov, Yu.M. Miroshnichenko, M.B. Smirnov, I.S. Kabanov, Micropor. Mesopor. Mater 61 (2003) 283.
[20] S.V. Goryainov, Eur. J. Mineral. 17 (2005) 201.
[21] G.D. Gatta, F. Nestola, T. Boffa Ballaran, Am. Mineral. 91 (2006) 568.
[22] S. Ori, S. Quartieri, G. Vezzalini, V. Dmitriev, Am. Mineral. 93 (2008) 53.
[23] P. Comodi, G.D. Gatta, P.F. Zanazzi, Eur. J. Mineral. 13 (2001) 497.
[24] G. Vezzalini, S. Quartieri, A. Sani, D. Levy, in: A. Galarneau, F. Di Renzo, F. Fajula, J. Vedrine (Eds.), Zeolites and mesoporous materials at the dawn of the 21st century, Studies in Surface Science and Catalysis, vol. 135, Elsevier Science B.V., Amsterdam, 2001, p. 09-P-09.
[25] P. Comodi, G.D. Gatta, P.F. Zanazzi, Eur. J. Mineral. 15 (2003) 267.
[26] O. Ferro, S. Quartieri, G. Vezzalini, E. Fois, A. Gamba, G. Tabacchi, Am. Mineral. 87 (2002) 1415.
[27] R. Arletti, O. Ferro, S. Quartieri, A. Sani, G. Tabacchi, G. Vezzalini, Am. Mineral. 88 (2003) 1416.
[28] E. Fois, A. Gamba, G. Tabacchi, R. Arletti, S. Quartieri, G. Vezzalini, Am. Mineral. 90 (2005) 28.
[29] E. Fois, A. Gamba, G. Tabacchi, S. Quartieri, R. Arletti, G. Vezzalini, in: A. Gamba, C. Colella, S. Coluccia (Eds.), Oxide Based Materials, Studies Surface Science and Catalysis series, vol. 155, Elsevier Science B.V., Amsterdam, 2005, p. 271.
[30] M. Colligan, P.M. Forster, A.K. Cheetham, Y. Lee, T. Vogt, J.A. Hriljac, J. Am. Chem. Soc. 126 (2004) 12015.
[31] R.M. Hazen, L.W. Finger, J. Appl. Phys. 56 (1984) 1838.
[32] M.D. Rutter, T. Uchida, R.A. Secco, Y. Huang, Y. Wang, J. Phys. Chem. Solids 62 (2001) 599.
[33] G.D. Gatta, S.A. Wells, Phys. Chem. Miner. 33 (2006) 243.
[34] C. Betti, E. Fois, E. Mazzucato, C. Medici, S. Quartieri, G. Tabacchi, G. Vezzalini, V. Dmitriev, Micropor. Mesopor. Mater 103 (2007) 190.
[35] S. Quartieri, G. Vezzalini, in: Proceeding of "Micro and mesoporous mineral phases" Accademia dei Lincei, Rome, December 6–7, 2004, p. 123.
[36] S. Ori, Ph.D. Thesis, University of Modena and Reggio Emilia, 2008.
[37] R.M. Barrer, E.A.D. White, J. Chem. Soc. (1951) 1267.
[38] I.S. Kerr, Z. Kristallogr. 139 (1974) 186.
[39] E. Krog Andersen, G. Ploug-Sorensen (Proceedings of the 7th IZC), Kodansha-Elsevier, Tokio, 1986, p. 443.
[40] P. Norby, A.N. Christensen, I.G. Krog Andersen, Acta Chem. Scand. A 40 (1986) 500.
[41] Ch. Baerlocher, W.M. Meier, D.H. Olson, Atlas of Zeolite Framework Types, Elsevier, The Netherlands, 2001.
[42] S. Quartieri, A. Sani, G. Vezzalini, E. Galli, E. Fois, A. Gamba, G. Tabacchi, Micropor. Mesopor. Mater 30 (1999) 77.
[43] E. Fois, G. Tabacchi, S. Quartieri, G. Vezzalini, J. Chem. Phys. 111 (1999) 355.
[44] E. Fois, A. Gamba, G. Tabacchi, S. Quartieri, S. Vezzalini, J. Phys. Chem. B 105 (2001) 3012.
[45] E. Fois, A. Gamba, G. Tabacchi, S. Quartieri, G. Vezzalini, Phys. Chem. Chem. Phys. 3 (2001) 4158.
[46] E. Fois, A. Gamba, G. Tabacchi, O. Ferro, S. Quartieri, G. Vezzalini, in: R. Aiello, G. Giordano, F. Testa (Eds.), Studies in Surface Science and Catalysis, vol. 142, Elsevier Sciences B.V., 2002, p. 1877.
[47] O. Ferro, S. Quartieri, G. Vezzalini, C. Ceriani, E. Fois, A. Gamba, G. Cruciani, Am. Mineral. 89 (2004) 94.
[48] C. Ceriani, E. Fois, A. Gamba, G. Tabacchi, O. Ferro, S. Quartieri, G. Vezzalini, Am. Mineral. 89 (2004) 102.
[49] P. Norby, Zeolites 10 (1990) 193.
[50] C. Ceriani, E. Fois, A. Gamba, Micropor. Mesopor. Mater 57 (2003) 73.
[51] C. Ceriani, A. Laio, E. Fois, A. Gamba, R. Martonak, M. Parrinello, Phys. Rev. B (2004). Art. No. 113403.
[52] R.A. Forman, G.J. Piermarini, J.D. Barnett, S. Block, Science 176 (1972) 284.
[53] H.K. Mao, J. Xu, P.M. Bell, J. Geophys. Res. 91 (1986) 4673.
[54] A.P. Hammersley, S.O. Svensson, M. Hanfland, A.N. Fitch, D. Häusermann, High Pressure Res. 14 (1996) 235.
[55] A.C. Larson, R.B. Von Dreele, GSAS-General Structure Analysis System, Report LAUR 86-748, Los Alamos National Laboratory, Los Alamos, New Mexico, 1994.
[56] B.H. Toby, J. Appl. Crystallogr. 34 (2001) 210.
[57] P. Thomson, D.E. Cox, J.B. Hastings, J. Appl. Crystallogr. 20 (1987) 79.
[58] L.W. Finger, D.E. Cox, A.P. Jephcoat, J. Appl. Crystallogr. 27 (1994) 892.
[59] R.J. Angel, EOS-FIT V5.2. Computer program. Crystallography Laboratory, Deparment of Geological Sciences, Virginia Tech, Blacksburg, USA, 2001.
[60] F. Birch, J. Geophys. Res. 57 (1952) 227.
[61] R. Car, M. Parrinello, Phys. Rev. Lett. 55 (1985) 2471.
[62] W. Kohn, L.J. Sham, Phys. Rev. A 140 (1965) 1135.
[63] A.D. Becke, Phys. Rev. A 38 (1988) 3098.
[64] J.P. Perdew, Phys. Rev. B 33 (1986) 8822.
[65] L. Kleinmann, D.M. Bylander, Phys. Rev. Lett. 48 (1982) 1425.
[66] N. Troullier, J.L. Martins, Phys. Rev. B 43 (1991) 1993.
[67] S. Nose', J. Chem. Phys. 81 (1984) 511.
[68] J. Hutter, M. Parrinello, et al., Computer code CPMD, <http://www.cpmd.org>. © IBM Research (Zurich) 1990–2001 and © MPI (Stuttgart) 1997–2001.
[69] E. Fois, A. Gamba, G. Tabacchi, J. Phys. Chem. B 102 (1998) 3974.
[70] E. Fois, A. Gamba, G. Tabacchi, Chem. Phys. Lett. 329 (2000) 1.
[71] P. Demontis, G. Stara, G.B. Suffritti, Micropor. Mesopor. Mater 86 (2005) 166.
[72] E. Spano, G. Tabacchi, A. Gamba, E. Fois, J. Phys. Chem. B 110 (2006) 21651.
[73] A. Alberti, E. Fois, A. Gamba, Am. Mineral. 88 (2002) 1.
[74] T. Yamanaka, T. Nagay, T. Tsuchiya, Z. Kristallogr. 212 (1997) 401.
[75] D.J. Weidner, Y. Huang, G. Chen, J. Hando, M.T. Vaughan, in: M.H. Manghnani, T. Yagy (Eds.), Properties of Earth and Planetary

Materials at High Pressure and Temperature, American Geophysics Union, Washington, DC, p. 473.
[76] Y. Fei, Y. Wang, in: R.M. Hazen, R.T. Downs (Eds.), High-temperature and High-pressure Crystal Chemistry, Rev. Mineral. Geochem. 41 (2000) 521.
[77] R.J. Angel, M. Bujak, J. Zhao, G.D. Gatta, S.D. Jacobsen, J. Appl. Cryst. 40 (2007) 26.
[78] W.H. Baur, in: M. Rozwadowski (Ed.), Proceedings of 2nd Polish–German Zeolite Colloquium, Nicholas Copernicus University Press, Torun, 1995, p. 171.
[79] R.J. Angel, in: R.M. Hazen, R.T. Downs (Eds.), High-temperature and High-pressure Crystal Chemistry, Rev. Mineral. Geochem. 41 (2000) 35.
[80] M.T. Dove, V. Heine, K.D. Hammonds, Miner. Magn. 59 (1995) 629.
[81] K.D. Hammond, V. Heine, M.T. Dove, Phase Transit. 61 (1997) 155.
[82] K.D. Hammond, H. Deng, V. Heine, M.T. Dove, Phys. Rev. Lett. 78 (1997) 3701.
[83] K.D. Hammond, V. Heine, M.T. Dove, J. Phys. Chem. B 102 (1998) 1759.
[84] M.T. Dove, K.O. Trachenko, M.G. Tucker, D.A. Keen, Rev. Mineral. Geochem. 39 (2000) 1.